Supporting Information

Rapid Scalable Processing of Tin Oxide Transport Layers for Perovskite Solar Cells

Joel A. Smith,[1] Onkar S. Game,[1] James E. Bishop,[1] Emma L.K. Spooner,[1] Rachel C. Kilbride,[1] Claire Greenland,[1] Rahul Jayaprakash,[1] Tarek I. Alanazi,[1,2] Elena J. Cassella,[1] Alvaro Tejada,[3,4] Ganna Chistiakova,[3] Michael Wong-Stringer,[1] Thomas J. Routledge,[1] Andrew J. Parnell,[1] Deborah B. Hammond,[5] David G. Lidzey.[1*]

1) Department of Physics & Astronomy, University of Sheffield, Sheffield, S3 7RH, UK
2) Department of Physics, College of Science, Northern Border University, Arar 73222, Kingdom of Saudi Arabia.
3) Helmholtz-Zentrum Berlin für Materialien und Energie GmbH, Institut für Silizium-Photovoltaik, Kekuléstraße 5, 12489 Berlin, Germany
4) Departamento de Ciencias, Sección Física, Pontificia Universidad Católica del Perú, Av. Universitaria 1801, Lima 32, Peru
5) Department of Chemistry, University of Sheffield, S3 7HF, UK.

*Corresponding Author – e-mail: d.g.lidzey@sheffield.ac.uk

Contents

Supplementary Figures

Supplementary Tables

Methods

Device fabrication

Materials: All materials were purchased from Sigma Aldrich unless otherwise specified. ITO coated glass substrates (Ossila, 20Ω/sq) were patterned using powdered Zn and 4 M diluted HCl. Substrates were cleaned by ultrasonication for at least 15 minutes in a 2% aqueous Hellmanex solution before rinsing extensively with DI water then acetone, sonicated for a further 15 minutes in IPA, dried with N_2 and UV ozone treated for 15 minutes.

Electron transport layer:

Tin oxide nanoparticle (np-SnO_2) electron transport layers were deposited from a colloidal solution (15 wt% in H_2O, Alfa Aesar) containing 1-2 nm particles in H_2O, stabilised by KOH (with a solution pH of ~11.5, Figure S18). We confirmed this solution to contain 20 wt% by evaporating the H_2O and calculating the mass loss. For spin coated SnO_2, this was diluted with DI water to 2.67% (6.5:1). This solution was statically spin coated at 3000 rpm for 30 s followed by annealing at 150 °C for 30 min.

Slot-die coated layers were deposited using an Ossila Slot Die Coater with a solution concentration of 6.5:1 H_2O:np-SnO_2. To ensure uniform coating two similar substrates were placed before and after the substrate to be coated (see Figure S4). A two-step flow process was programmed, with the first step controlled to dispense a uniform meniscus, at a coating speed of 0.5 mm s^{-1} and a flow rate of 30 μl s^{-1}. The second step then dispensed this over the substrate area, with a coating speed of 3-15 mm s^{-1} and a flow rate of 2 μl s^{-1}. The substrate temperature was held at 80 °C throughout with a gap height of 150 μm.

Spray-coated SnO_2 layers were deposited using a Prism Ultra-coat 300 system (Ultrasonic Systems Inc.) which is operated in low humidity conditions. Head speeds between 120-180 mm s^{-1} (Figure S5) were used at a head height of 30 mm, with pressure ~10 mbar, on a hot plate at 20 °C. Solution concentration was optimised to a volume ratio of 1:70 SnO_2 NPs:H_2O (17.5 ml H_2O + 250 μl NPs), corresponding to a solution concentration of 0.29 wt% (using 20 wt% calculated above). For the mixed IPA:H_2O np-SnO_2 system used in devices, 5 ml of IPA was added by dropwise addition to a solution containing 12.5 ml H_2O and 250 μl np-SnO_2 solution. In all cases, np-SnO_2 was removed from the ITO in the metal contact evaporation area by fine swabbing with H_2O. Where used, the Hot Air Flow (HAF) heating was performed used a 2000 W Heat Gun (Tacklife HGP73AC) operating at ~120 ± 10 °C determined using a thermocouple attached to a test substrate.

Where used, the sol-gel SnO_2 spin-coating process was completed exactly following the method outlined by Ke $et\ al.$ and Anaraki $et\ al.$[1,2] Briefly, $SnCl_4.5H_2O$ in IPA is spin coated at 3000 rpm, followed by drying at 100°C and annealing at 180°C.

Prior to perovskite deposition, SnO_2 layers were UV ozone cleaned (Ossila UV ozone cleaner with no O_2 flow) for 15 minutes before transferring to a nitrogen glovebox. Where used, O_2 plasma treatment was performed for 5 minutes in a custom-built chamber with pressure 2 mbar that was flushed with O_2 three times before treating for 5 minutes at approximately 400 W.

Perovskite: Triple-cation perovskites were deposited via the one-step deposition method from a precursor ink containing (per ml of solvent, not accounting for volume change) FAI (1M, Ossila), MABr (0.2M, Ossila), PbI_2 (1.1M, TCI) and $PbBr_2$ (0.2M, TCI) in fresh anhydrous DMF/DMSO (4:1 volume ratio) with 50 μl of a 1.5M CsI solution in DMSO added per ml to give the desired solution composition $Cs_{0.05}FA_{0.79}MA_{0.16}PbI_{2.45}Br_{0.55}$. The solution was heated to 65 °C for 15 minutes to aid dissolution if required. Films were spin coated statically in a two-step program: 1000 rpm for 10 s then 6000 rpm for 20 s with 100 μl of chlorobenzene antisolvent dripped on the film around 5 s before the end, with the film immediately turning translucent brown when using Cs. Films were then transferred to a hotplate for annealing at 100 °C for 60 min. In measurements where perovskite layers were prepared for optical characterisation, films were simply deposited using the above protocol on cleaned, UV-ozone treated quartz-coated glass substrates.

Hole transport layer/contact: Spiro-OMeTAD hole transport layer was deposited from a solution containing 86 mg ml⁻¹ spiro-OMeTAD (sublimed 99.5%, Ossila) in chlorobenzene. To each 1 ml was added 34 μl of 4-tert-butyl-pyridine (tBP, 96.6%), 20 μl of lithium bis(trifluoromethanesulfonyl)imide solution (LiTFSI, 500 mgml⁻¹ in acetonitrile) and 11 μl of FK209 solution (FK209 Co(II) PF6, Dyesol, 300 mg ml⁻¹ in acetonitrile). This solution was vortex mixed and filtered before spin-coating dynamically at 4000 rpm for 20 s. Layers were partially removed using a razor blade to pattern devices before 80 nm of Au (Cooksongold) was thermally evaporated under high vacuum as the electrode (area 0.25 cm²) with one cell created per substrate unless otherwise stated.

Characterisation

Current-voltage measurements: J-V curves were used to determine device performance under ambient conditions using a Newport 92251A-1000 solar simulator. Prior to testing, an NREL certified KG5 filtered silicon reference cell was used to calibrate the simulated AM1.5G light to 100 mWcm⁻² at the sample location. A sample holder was used to ensure consistent positioning and illumination. A

metal illumination aperture mask defined a cell area of 0.155 cm^2 (accurately determined using optical microscope and ImageJ area analysis) to compensate for any geometric distortion in the electrode evaporation. J-V measurements were recorded using a Keithley 237 source measure unit sweeping between -0.1 and 1.2 V at 100 mVs^{-1} with all performance metrics extracted from the curve. Stabilised power output measurements were taken by holding the devices for several minutes at a bias voltage defined by the reverse sweep V_{mpp}. J-V scans were typically recorded on the second or third day after device fabrication and no light-soaking or voltage pre-biasing was used.

X-ray scattering: Grazing incidence X-ray scattering was performed using a Xeuss 2.0 (Xenocs) system with 9.243 keV X-rays from a liquid Ga MetalJet source (Excillum). X-rays were incident on the sample surface, which were 100 nm thick np-SnO$_2$ with various heat treatments, at an angle of 0.32°. The sample and flight tube were held under vacuum during operation to remove background scatter. Scattered X-rays were then detected with a PILATUS3R 1M (DECTRIS), with a sample to detector distance of ~300 mm. This data was corrected, reduced and reshaped using the GIXSGUI MATLAB toolbox.[3] For GISAXS profile fitting, a shape independent Guinier-Porod fitting model was applied using SasView,[4] with further details given in SI Note 3.

Scanning electron microscopy: Device cross-section images were recorded from films using a Carl Zeiss-modified Raith Nanofabrication SEM operating at a beam energy of 1.5 kV at a working distance of 2-3 mm with backscattered electrons collected with an in-lens detector.

Light V$_{OC}$: Oriel LSH-7320 ABA LED solar simulator with ability to control illumination intensity between 0.1 Sun to 1.1 Sun was used to perform intensity depended V$_{OC}$ and transient photovoltage measurements. V$_{OC}$ was measured as a function of time using Keithley 2420 meter controlled through LabTracer 2.9. In our analysis, we use a fitting relation from a modified ideal diode equation for an illuminated cell operating at V$_{OC}$[5]; $eV_{OC} = E_{gap} - n_{ID}k_B T ln\left(\frac{I_0}{I}\right)$.

Atomic force microscopy: AFM measurements were performed in tapping mode using a scanning force microscope (Veeco Dimension 3100) with a nanoscope 3A feedback controller. The AFM tips were TESPA-V2 probes (Bruker) with a resonance of around 320 kHz and spring constant of 42 N/m. Gwyddion 2.54 software was used to process the AFM images and roughness values were calculated using the Gwyddion statistical quantities tool.

Profilometry: A Bruker DektakXT profilometer was used to investigate the morphology of completed devices. Here, 2 x 2 mm map profiles were collected at a 1 μm line resolution. Data was processed by cropping for touchdown error, plane levelling to remove tilt from stage, base flattening and step line correcting in both x and y.

Spectroscopic ellipsometry: A M2000v ellipsometer (J.A. Woolam Co.) was used to determine the thickness of np-SnO_2 thin films deposited on silicon substrates (Ossila Ltd). Using CompleteEASE software, a Cauchy model was fitted to Ψ (the ratio of the incident and reflected amplitudes) and Δ (the ratio of the phase difference of the incident and reflected light) over the wavelength range where the films are optically transparent (500-1000 nm).

SnO_2 E_{gap} determination (ellipsometry and transmission): Optical measurements were performed with a Sentech SE850 ellipsometer (210-850 nm) and a Perkin Elmer Lambda 1050 spectrophotometer (transmission, 250-700 nm). The complex refractive index was obtained self-consistently for each individual wavelength using the combined ellipsometry and transmission data via a global error minimization.[6] The resulting absorption coefficient was fitted with a band fluctuations model which describes the direct absorption edge and Urbach tail in a single equation.[6,7]

Transmission measurements: Measurements were performed using an Andor Shamrock SR-193i-A double-grating imaging spectrograph, with a focal length of 0.193 m. The spectra were recorded using a 150 grooves/ mm grating blazed at 500 nm. The collimated white light from a custom-built tungsten lamp source was focused on to a vertically mounted sample at normal incidence. The transmitted light was then collimated using a 50X Mitutoyo Plan Apo SL infinity corrected objective and focussed into the spectrometer using a final collection lens. These were converted to absorbance units using the relation $A = 2 - \log(T)$. Perovskite layer thickness was determined to be approximately 500 nm using profilometry and confirmed using SEM cross-section, from this absorption coefficients were calculated using $\alpha = 2.303(A/t)$ for Tauc plots used for E_{gap} determination.

Photoluminescence: Measurements were performed using an Andor Shamrock SR-303i-A triple-grating imaging spectrograph, with a focal length of 0.303 m. The spectra were recorded using a 150 grooves / mm grating blazed at 500 nm. The horizontally mounted collection arm of a goniometer was employed to measure the emission at around normal incidence following excitation from a 400 nm diode laser, which was directed to the sample using a vertically displaced arm such that the angle of incidence was ~ 15°. The PL was collected using a pair of lenses on the collection arm which was then fibre coupled into the spectrometer. All samples were collected at five locations with data presented averaged across all locations. To determine optical E_{gap}, an exponentially modified Gaussian (EMG) function was fitted to the data, with peak values given in Table S5.

X-ray photoelectron spectroscopy: XPS data was collected using a Kratos AXIS Supra under UHV conditions (~10^{-9} mbar). Monochromated aluminium radiation (1486.6 eV) of power 225 Watts was used to collect XPS survey scans (wide scans) with a pass energy of 160 eV, between 1200 to 0 eV at 1 eV intervals and 300 seconds sweep time. High-resolution XPS spectra were collected over the C 1s, O

1s, Sn 3d, In 3d and Sn valence band regions at 20 eV pass energy, 0.1 eV intervals and one sweep of 300 seconds over an appropriate energy range. Samples were clamped to the sample bar using a contact to provide a conductive path from the top surface to the sample holder. Charge neutralisation was not used. The area analysed was 700 μm by 300 μm, and two areas per sample were collected. The data was primarily analysed using CasaXPS and OriginPro software. A transmission function characteristic of our Supra instrument is attached to the data by the Kratos software and subsequently used by the Casa software. The sensitivity factors used are the theoretical Scofield factors adjusted for the variation in mean free path with kinetic energy. No correction for angular distribution was made as the angle between the sample and the X-ray source on the Supra is 54° (the magic angle). Analysis and fitting of the XPS elemental core level spectra was conducted using Fityk.[8] The spectra for the same core levels with different post-treatments were fitted simultaneously using Voigt profiles with coupled Gaussian and Lorentzian line widths with linear background subtraction. For the O 1s peaks, the FWHM was locked relative to the first region for all bonds, and the distance between peaks was fixed.

Ultraviolet photoelectron spectroscopy: UPS was carried out using the Kratos AXIS Supra with the HeI (21.22 eV) emission line employed for excitation. The samples were mounted as described above. The data were acquired at a bias of −9V, from an area that was 110 μm in diameter, at 10 eV pass energy, 0.025 eV energy resolution over an appropriate energy range for one 300 second sweep. UPS data was also collected from an Au foil control sample mounted with the samples to confirm the measured Fermi energy level for a metal sample was 0 eV.

Note 1 – Solvent mixtures

Improved wetting of the np-SnO$_2$ system for slot-die coating has been achieved by diluting with ethanol by dropwise addition.[9] Without dropwise addition, the colloidal suspension is unstable and aggregates form when mixing with isopropanol or ethanol and demixing occurs during the spray process as discussed in the main text (Figure S10).

We conducted initial investigations to improve wettability using a range of other low surface tension polar solvents, as well as with additional KOH to modify the np-SnO$_2$ stabilisation. Whilst improved wetting and a metastable solvent:H$_2$O ratio was achieved with acetonitrile (ACN), the system reacted with KOH over 24 hours causing aggregates to form. It is likely that the low concentration KOH base is catalysing hydrolysis of the ACN to various degradation products - likely ammonia, then acetamide and acetic acid.[10] Having a mixed solvent system also leads to two phase drying, which can lead to further layer inhomogeneity, causing thicker regions of material to form.[11] Consequently, the requirements for an ideal second solvent here are:

1) Low surface tension for enhanced wetting.
2) Low boiling point for more rapid drying.
3) Miscibility with water.
4) Chemical stability in the presence of KOH.
5) Reduced basicity than KOH to ensure no competition for np-SnO$_2$ suspension.
6) In an ideal case, a continuous azeotrope with H$_2$O to lower the boiling point.

Note 2 – Optical E$_{gap}$ determination

Bandgap values are commonly determined from the absorption coefficient by extrapolating from the region of the absorption edge where the parabolic band approximation is valid. For direct semiconductors, this region behaves linearly in a $(\alpha E)^2$ vs. E plot, and so the intercept of a linear fit with the horizontal axis yields the optical E$_{gap}$. This type of procedure was originally developed for amorphous materials, for which it is commonly known as a Tauc plot.[9]

This approach has two limitations. Firstly, the selection of the appropriate data points for the fit is somewhat arbitrary and it can be challenging to differentiate the parabolic band edge from the Urbach tail and higher order absorption regions. Secondly, if the Urbach tail is large, there may only be few or no suitable data points available for the linear fit. In these cases, calculated E$_{gap}$ values can be strongly affected by which points are used. Consequently, it is advantageous to use a procedure that considers both the Urbach tail and parabolic band edge regions, which significantly increases the number of available points and reduces the human error involved in their selection. For this reason, bandgap values are extracted by fitting the absorption coefficient with a band fluctuations model that considers both the Urbach tail and parabolic band edge in a single equation,[7] and has the following form:

$$\alpha(E) = -\frac{\alpha_0}{E}\sqrt{E_u}\,\mathrm{Li}_{1/2}\left(e^{\frac{E-E_{\mathrm{gap}}}{E_u}}\right)$$

where α_0 is a constant, $\mathrm{Li}_{1/2}(x)$ is the $1/2$-order polylogarithm function of x, E_{gap} is the optical bandgap and E_u is the Urbach energy. Our measurements of absorption (assuming direct E_{gap} behaviour) indicate values of 4.44 and 4.4 eV for non-annealed and annealed np-SnO$_2$ films respectively (see Figure S12). We have also performed spectroscopic ellipsometry that indicate similar values. The unexpectedly high values of E_{gap} for np-SnO$_2$ could be explained by partial incorporation of organic contaminants into the film. Alternatively, film porosity through voids between joined nanoparticles could lead to a lower effective absorption coefficient, which might then modify the apparent optical E_{gap} values. As such, the E_{gap} values reported are considered an approximation.

Note 3 – GISAXS modelling

We prepared 100 nm thick films (confirmed by ellipsometry on SiO$_2$), and calculated the approximate critical angle (θ_C) for SnO$_2$ at a photon energy of 9.243 keV to be 0.32°.[12] By working close to the critical angle for SnO$_2$ and taking in-plane line-cuts (integrating $0 \leq Q_z \leq 0.2$ Å^{-1}) through the data, we are able to probe the lateral structure of the film surface, as an aggregate measurement of the whole film. With no well-defined length scales apparent in the small-angle data (as would be indicated by defined scattering features), an approach using a shape-independent fitting model was required. Here, the so-called radius of gyration (R_G) is a measure of the characteristic length scale within the film. Considering the nanoparticles as spheres, we fitted an empirical Guinier-Porod model[13] to our data, of the form:

$$I(Q) = \begin{cases} G/Q^s \, exp\left(\dfrac{-Q^2 R_G^2}{3-s}\right) & for\ Q \leq Q_1 \\ D/Q^d & for\ Q \geq Q_1 \end{cases}$$

where G and D are the Guinier and Porod scale factors, d is the Porod exponent (which describes the smoothness of particle surfaces), s is a dimensionality parameter to describe the particle shape and Q_1 is the continuity region between the Guinier and Porod regimes:

$$Q_1 = \frac{1}{R_G}\left[\frac{(d-s)(s-3)}{2}\right]^{1/2}$$

This model can therefore be used to probe the shape of, and interfaces between, domains within the film. From the data presented in the main text and in Table S3, it can be seen that R_G increases during annealing and from this we can use the relation for spherical bodies with radius R, $R_G{}^2 = \frac{3}{5}R^2$, to calculate sizes of the spherical film domains. In all cases, this is valid as fitting for s in the above model tended to 0, so any deviation from spherical particle shape is within the margin of error.
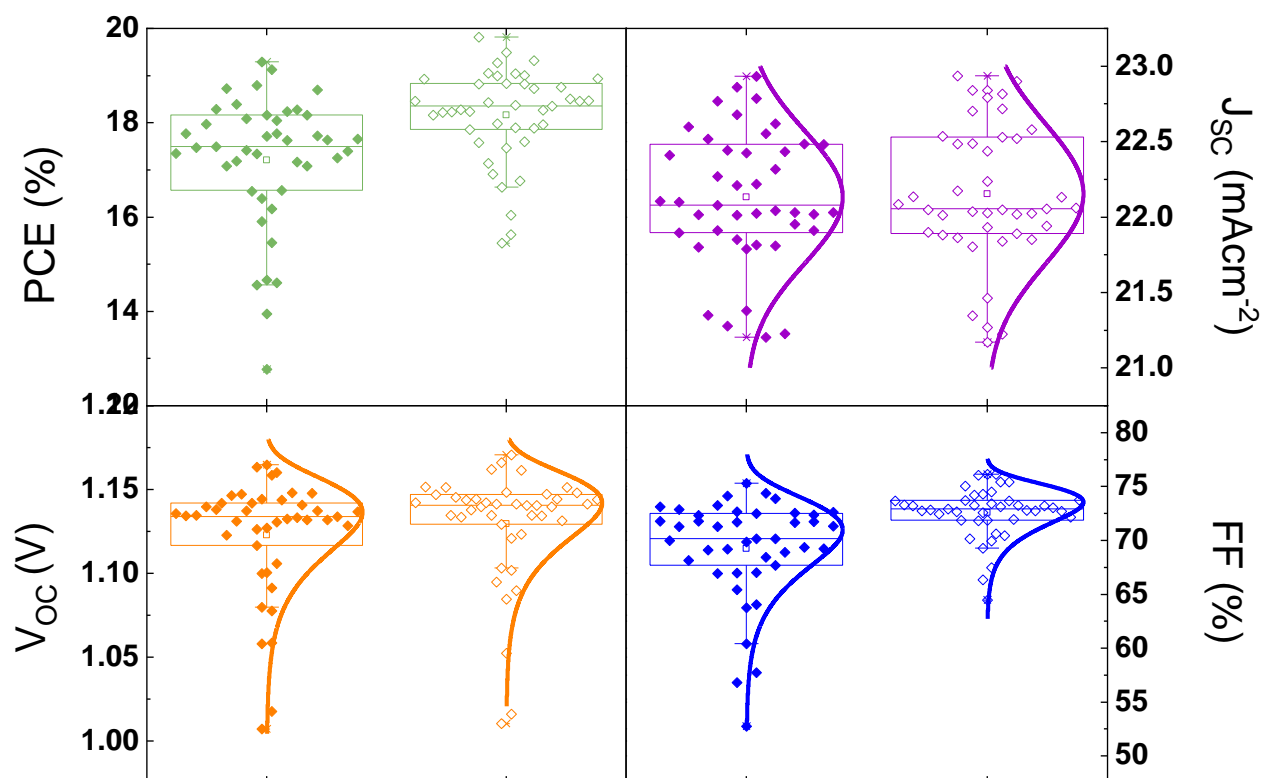
Figure S1: All reverse (hollow, right) and forward (filled, left) sweep device metrics for spin coated np-SnO$_2$ devices, showing excellent reproducibility between batches of devices.
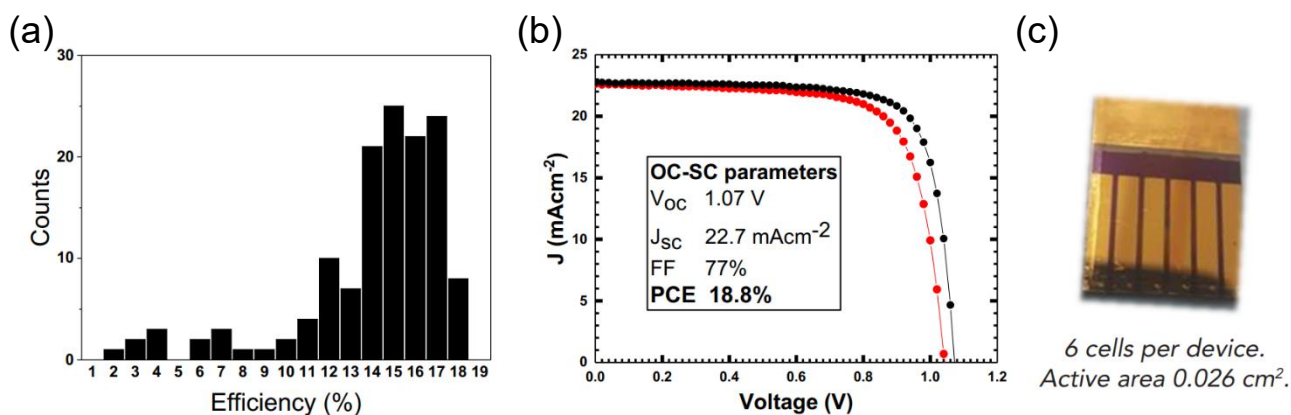
Figure S2: Performance of all functioning small area np-SnO$_2$ perovskite devices on FTO substrates with architecture FTO/np-SnO$_2$/perovskite/spiro-OMeTAD/Au. a) Histogram of device efficiencies (reverse sweep), b) J-V curve for champion cell, c) image of complete device with 6 small cells per substrate. The greater performance variation compared to ITO cells (Figure 1c) could be due to the higher roughness of FTO, which may lead to pinholes through the ETL layer. Alternatively, with the smaller cell layout used here, fabricated cells may have a broader PCE distribution due to np-SnO$_2$ thickness variation over the substrate surface. We note that recent work has confirmed that np-SnO$_2$ is highly thickness tolerant, with thicker layers on FTO substrates still resulting in highly efficiency devices.[9]
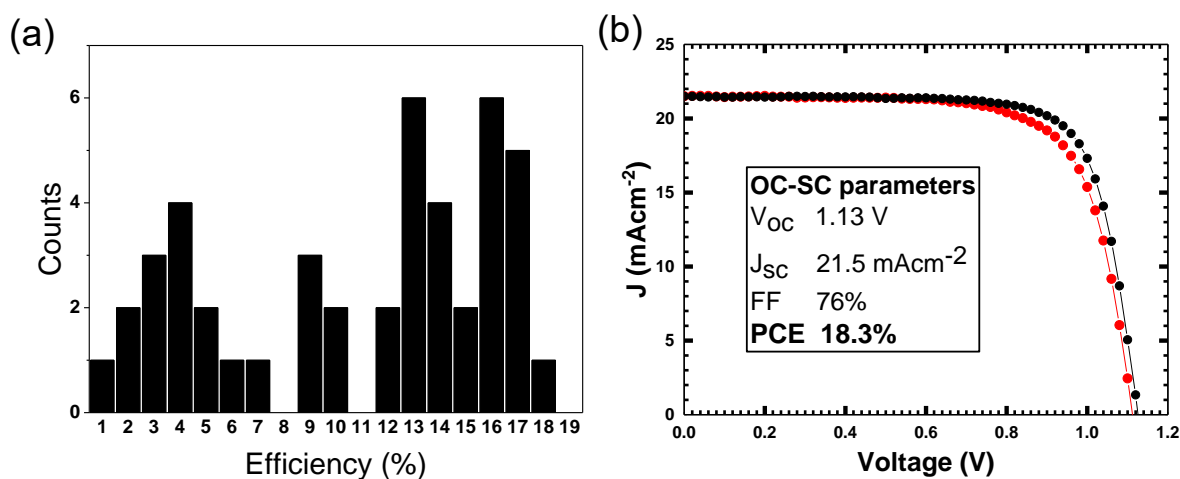

Figure S3 Device performances for small area devices using spin-coated SnCl$_4$.5H$_2$O method based on the architecture FTO/np-SnO$_2$/perovskite/spiro-OMeTAD/Au. a) Histogram of reverse sweep efficiencies and b) *J-V* curve of the champion device. Significant performance variation is observed compared to FTO/np-SnO$_2$, as well as requiring a longer and higher temperature deposition protocol.
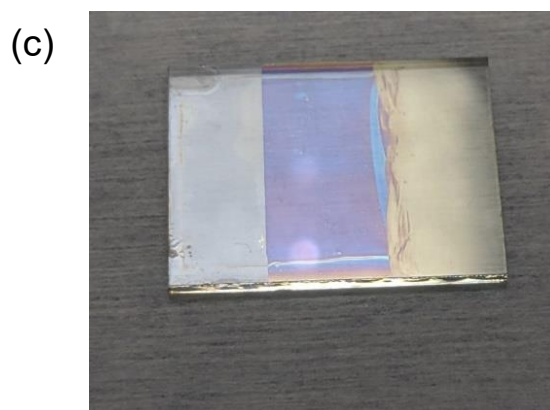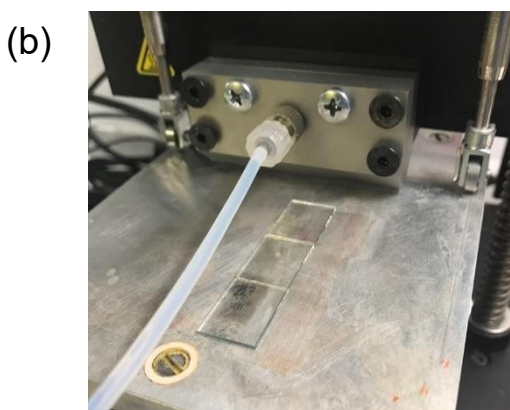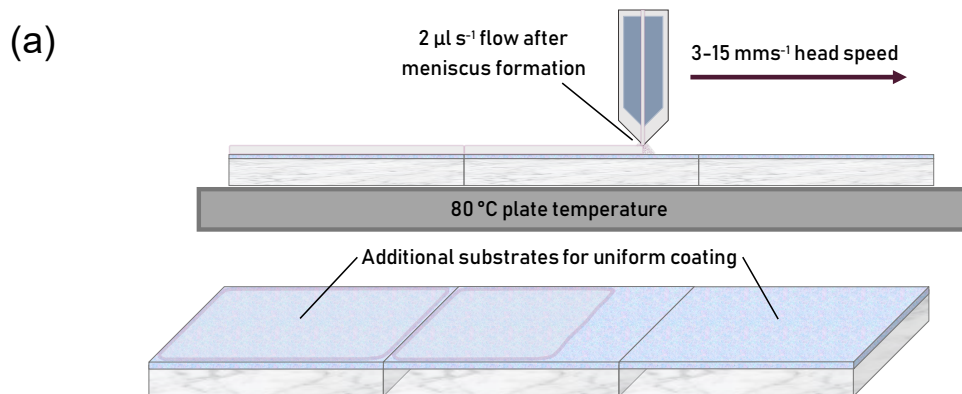
Figure S4: a) Scheme illustrating slot-die coating process. b) Layout during slot-die coating with additional substrates to ensure uniform coating of the central substrate. c) Typical slot-die coated film with np-SnO$_2$ layer removed at one side for top contact evaporation.
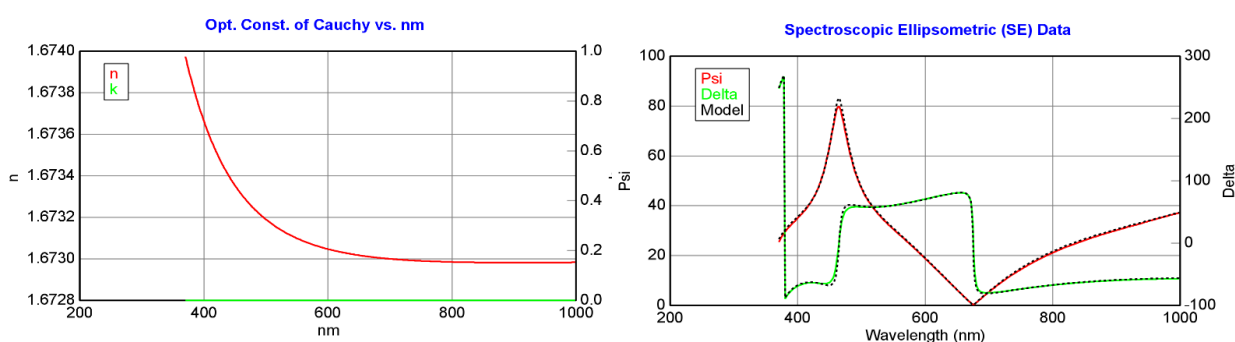
Figure S5: Typical spectroscopic ellipsometry data and Cauchy model fitting for spray-coated np-SnO$_2$ layers (here 19.01 mm). Approximate layer thicknesses on SiO$_2$ substrates were found to be 17.67 ± 3.41 for spray-coated cells (N = 5) and 38.21 ± 8.44 for slot-die coated (N = 2). The values given here are considered estimates, as the wetting behaviour of np-SnO$_2$ on SiO$_2$ will differ from that on ITO (see also note in Table S1).
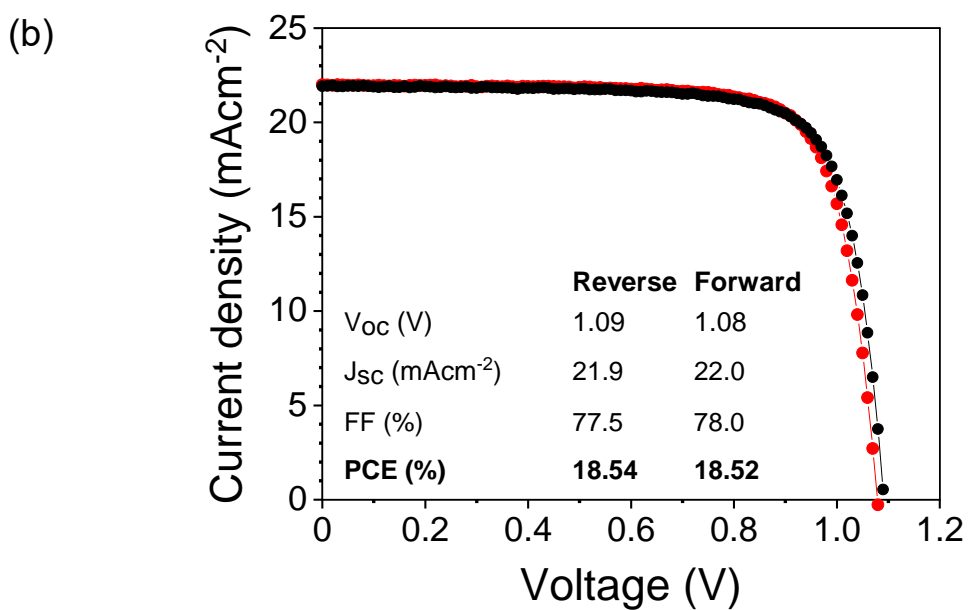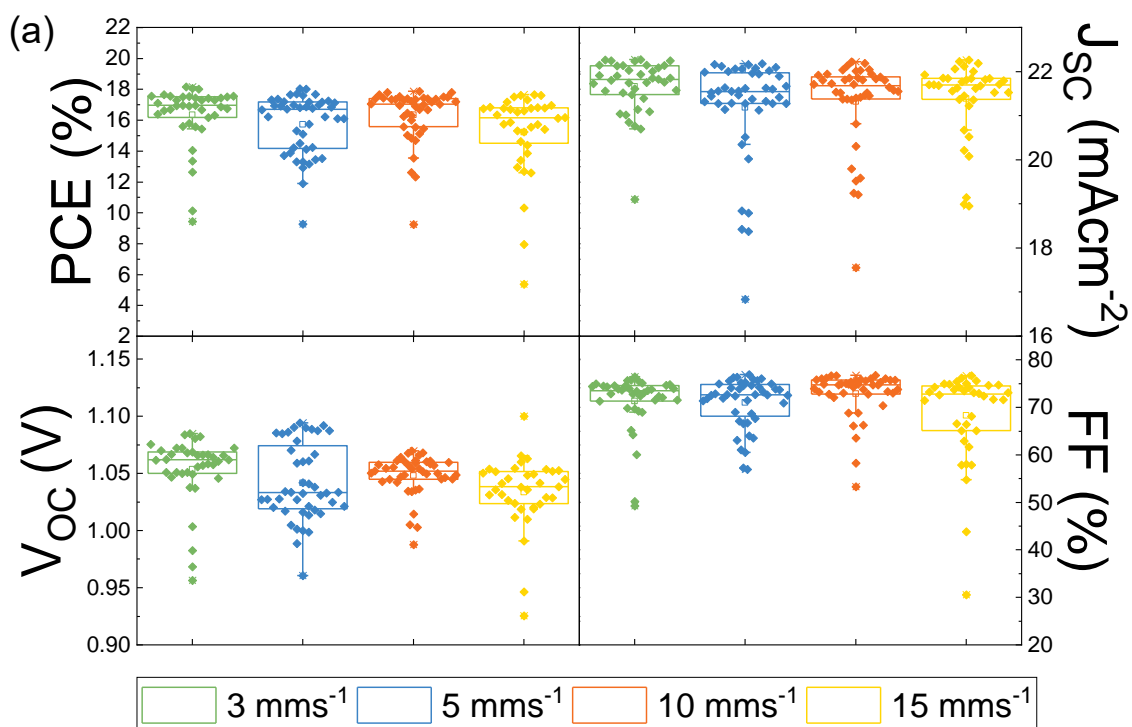
Figure S6: a) Device performance metrics for all slot-die coated np-SnO₂ layers showing comparable efficiencies and parameters across a range of coating speeds. b) J-V curve of the champion slot-die coated cell.

Electron transport layer	Treatment	Sweep	PCE (%)	J_{SC} (mAcm^{-2})	V_{OC} (V)	FF (%)	No. of cells
FTO/np-SnO$_2$ (Spin-coat)	Annealed + 15 mins UVO	Forward	17.19 (13.65±2.73)	22.62 (21.56±1.36)	1.04 (1.02±0.05)	72.94 (61.80±9.02)	78
		Reverse	18.80 (14.07±3.96)	22.75 (21.77±1.31)	1.07 (1.02±0.13)	77.05 (61.76±13.11)	
FTO/SnO$_2$ (SnCl$_4$.5H$_2$O)	As per methods	Forward	17.27 (11.07±3.94)	21.50 (20.82±1.13)	1.11 (0.88±0.19)	72.23 (57.79±12.02)	56
		Reverse	18.33 (10.38±6.10)	21.50 (20.77±1.19)	1.13 (0.82±0.33)	75.73 (53.85±19.54)	
ITO/np-SnO$_2$ (Slot-die)	Annealed + 15 mins UVO	Forward	18.52 (16.47±1.66)	22.00 (21.51±0.79)	1.08 (1.05±0.03)	78.04 (73.08±4.91)	79
		Reverse	18.54 (15.55±2.54)	21.92 (21.31±1.07)	1.09 (1.05±0.03)	77.48 (69.26±8.07)	

Table S1: Cell performance for all operational small area cells shown in Figures S2, S3 and S6, with FTO/np-SnO$_2$, FTO/SnO$_2$ (tin chloride pentahydrate conversion route) and slot-die coated ITO/np-SnO$_2$ cells. Slot-die cells are found to exhibit reduced V_{OC} compared to spin-coated devices, however the different cell architectures may lead to such variations. Variations in performance may also be result from non-uniformity in the SnO$_2$ layer thickness across the substrate area.
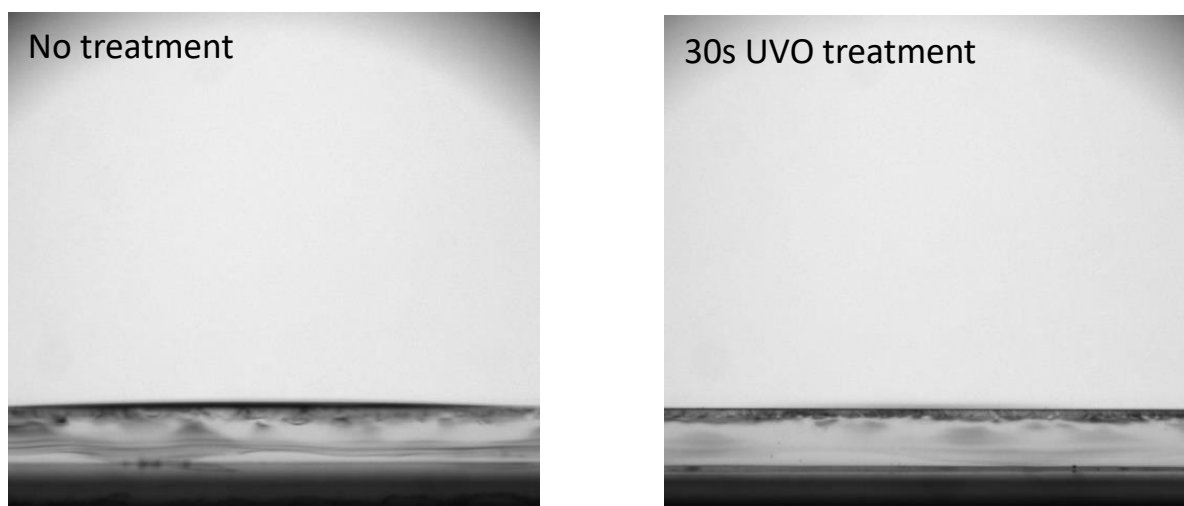

Figure S7: Contact angle measurement showing good wetting of an H$_2$O droplet on ITO after cleaning procedure (finishing with IPA sonication and N$_2$ drying) and perfect wetting after a further 30s UVO treatment.
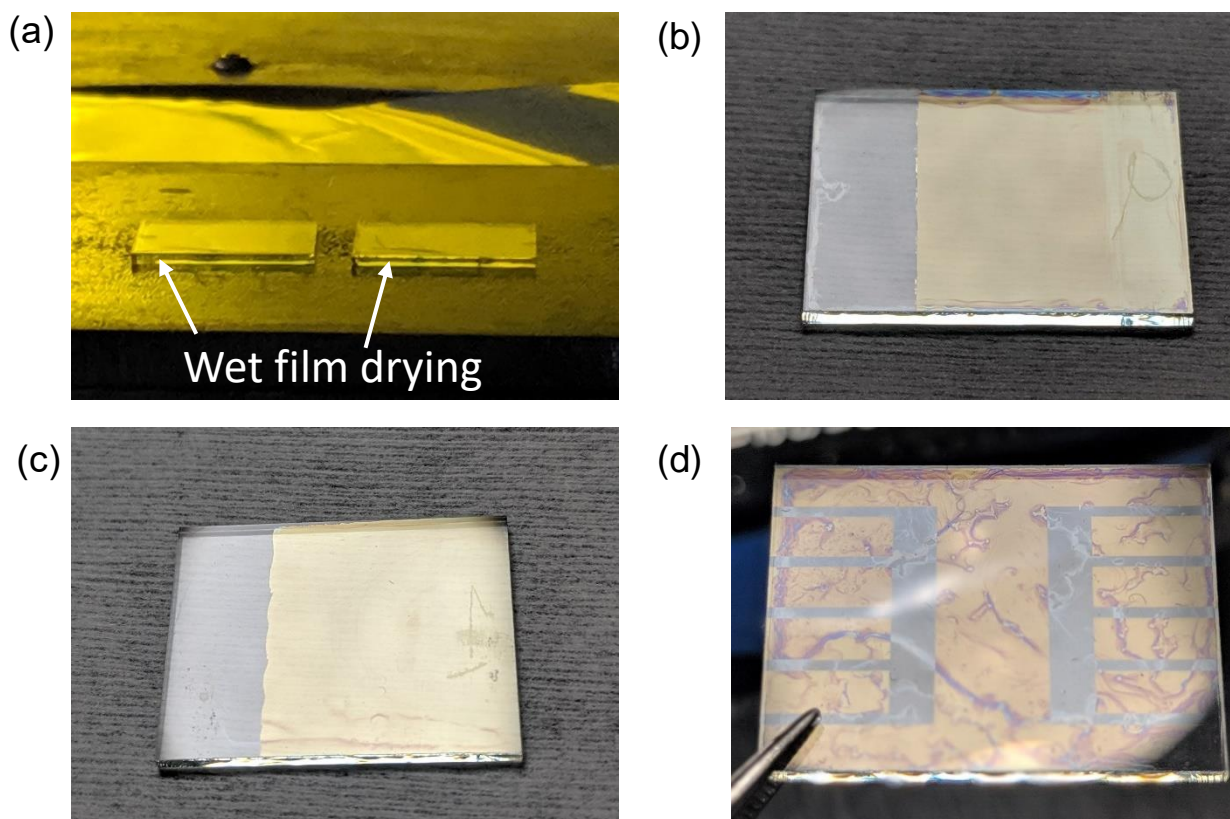
Figure S8: Photographs of spray-coated np-SnO₂. a) Photograph during sequential drying, with wet film receding to one corner. b) Typical np-SnO₂ film with uniform layer formation. Here np-SnO₂ is removed on the right for Au to contact to ITO, with perovskite/spiro-OMeTAD subsequently removed by razor blade. C) np-SnO₂ layer with insufficient UV ozone treatment prior to deposition and d) with higher solution concentration than the optimised 1:70 dilution, both leading to inhomogeneous mottled films.
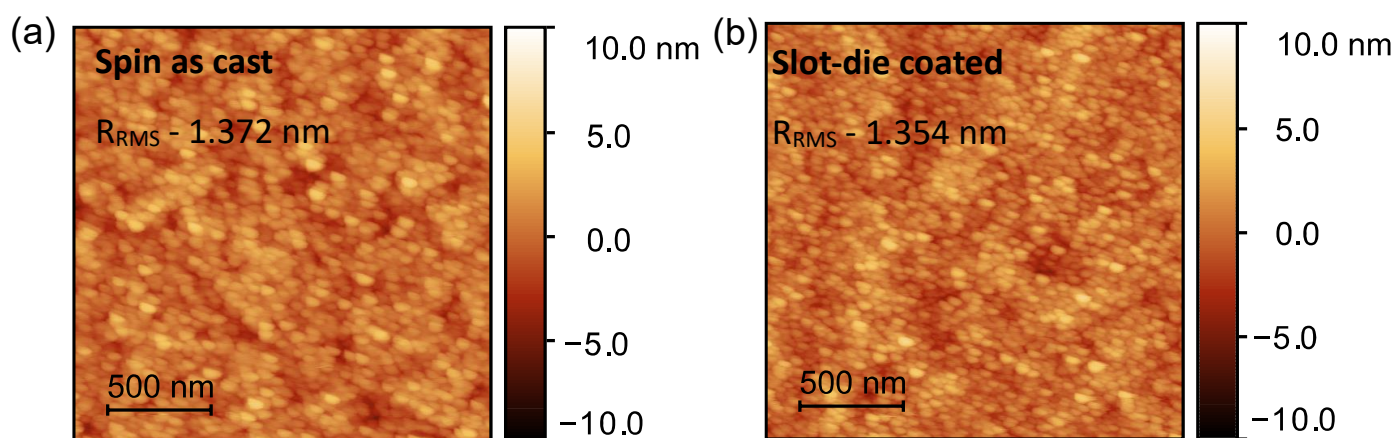
Figure S9: AFM height topography of a) spin-coated np-SnO₂ before annealing and b) slot-die coated np-SnO₂. The SnO₂ film exhibits slightly decreased roughness following annealing.
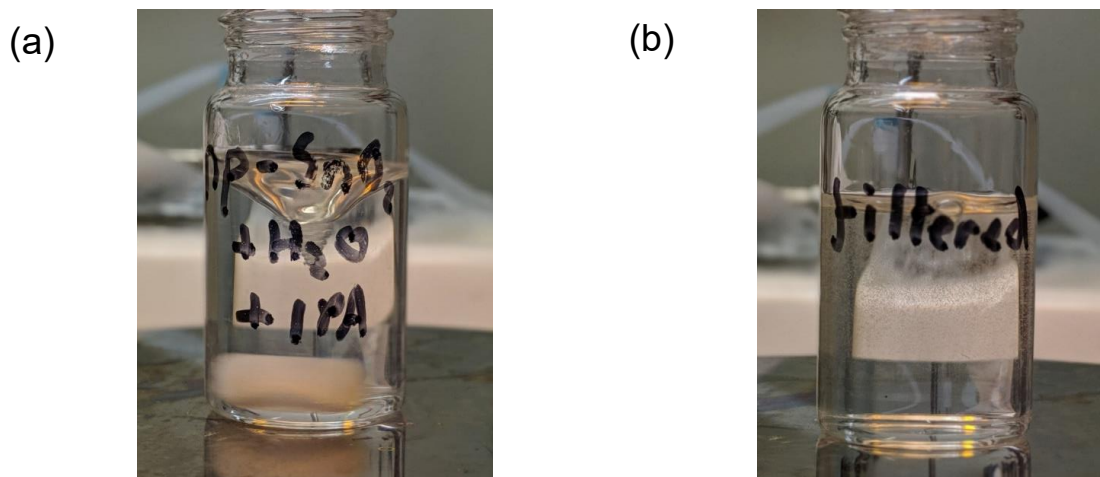
Figure S10: np-SnO₂ solution containing 1 ml of 20 wt% np-SnO₂, 5 ml H₂O and 5 ml IPA (added dropwise) a) before and b) after filtering through a PVDF filter, mimicking the atomisation in the ultrasonic spray coater. Here the IPA/H2O solvent de-mixes, leading to regions of aggregation in the as-sprayed np-SnO₂ film.
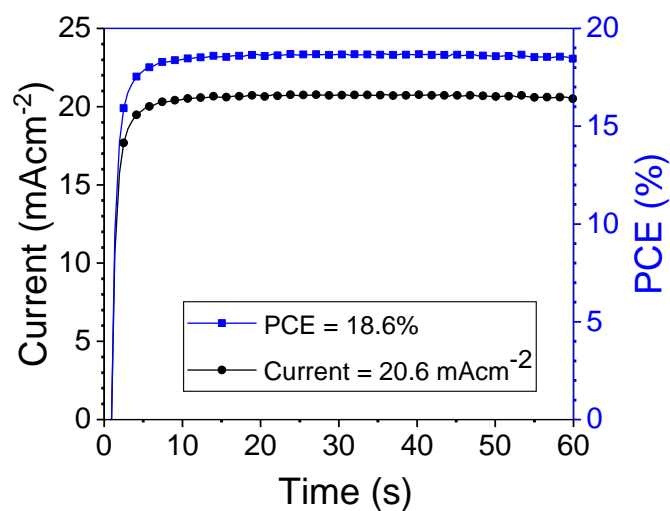
Figure S11: Stabilised power output for the champion spray-coated np-SnO₂ device.

Sample	Thickness (nm)	E_{gap} (SE, eV)	E_{gap} (Tauc, eV)	E_U (meV)
As deposited	94.69	4.476	4.433	159
Annealed	101.42	4.446	4.391	144

Table S2: Optical E_{gap} determination from Tauc plots (shown in Figure S12) and fitting to combined spectroscopic ellipsometry (SE) and transmission data. From the modelling to the SE data described in SI Note 2, the Urbach energy (E_U) is also determined. The thickness value here for the annealed films (on quartz) is in good agreement with that determined for films on SiO_2 in the process design of 100 nm layers for GISAXS measurements (SI Note 3).

(a) (b) (c)

Figure S12: Optical E_{gap} determination for np-SnO_2. a) Tauc plots for as deposited and annealed np-SnO_2 from transmission measurements. b) Corresponding real (n) and imaginary (k) complex refractive index components from fitting to spectroscopic ellipsometry (SE) and transmission (T) data. c) Tauc plot using $\alpha = \frac{2\pi k}{\lambda}$ for combined SE and T data, with the band fluctuation model fit overlaid.

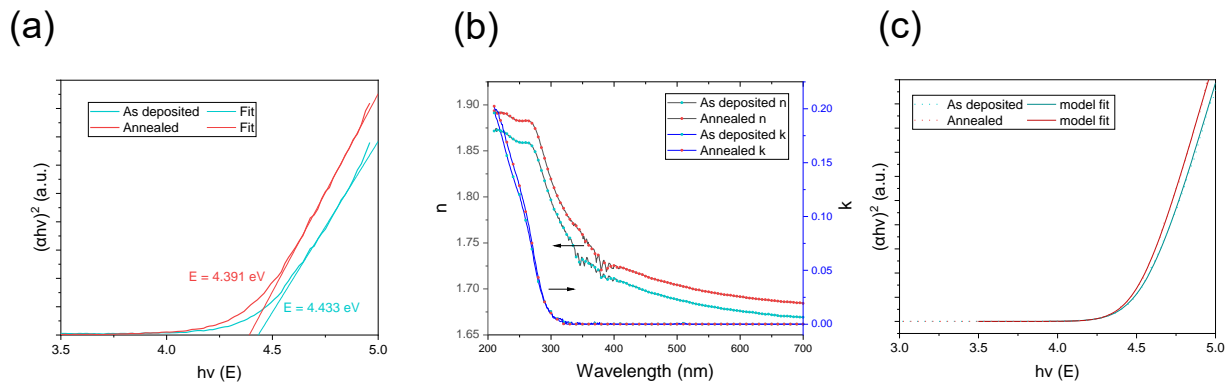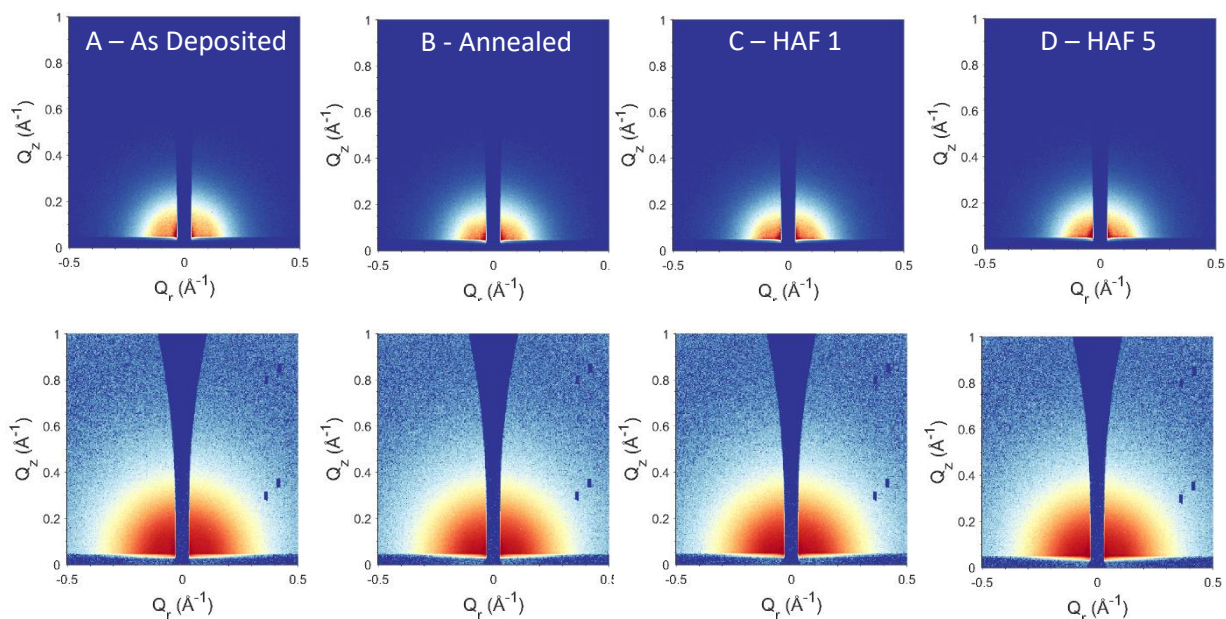**Figure S13:** 2D GISAXS scattering patterns with linear (top) and log (bottom) intensity plot scales for four np-SnO$_2$ annealing conditions. In-plane cuts through this data are shown in Figure 4.

| Sample | Fit parameters | | | Repeated from Table 2 | | |
	Scale	Background	Q$_1$	R$_g$ (Å^{-1})	d (Porod exponent)	Grain radius
As deposited	286.49 ± 1.08	0.00 ± 1.25	0.2468	9.09 ± 0.05	3.984 ± 0.31	1.173 ± 0.006
Annealed	267.44 ± 1.12	0.00 ± 1.20	0.269	9.43 ± 0.05	3.612 ± 0.24	1.218 ± 0.006
HAF 1	279.60 ± 1.10	0.00 ± 1.22	0.2586	9.27 ± 0.05	3.829 ± 0.28	1.197 ± 0.006
HAF 2	290.96 ± 1.09	0.00 ± 1.21	0.2575	9.31 ± 0.05	3.831 ± 0.27	1.202 ± 0.006
HAF 5	276.95 ± 1.11	0.00 ± 1.20	0.2487	9.42 ± 0.05	3.661 ± 0.24	1.216 ± 0.006

Table S3: Extended fit parameters and Q$_1$ for Guinier-Porod fitting model applied to GISAXS linecuts. Full details are given in SI Note 3.

Figure S14: Photo of heat gun setup used for HAF annealing. Temperature was stabilised to 120 ± 10 °C, confirmed with a thermocouple connected to a suspended substrate, matching the conditions during HAF annealing.

Annealing	Treatment	Sweep direction	PCE (%)	J_{SC} (mAcm^{-2})	V_{OC}	FF	No. of cells
Air dried	None	Forward	17.59 (16.70 ±0.74)	22.69 (22.39 ±0.16)	1.11 (1.11 ±0.01)	70.09 (67.30 ±2.30)	9
		Reverse	18.56 (17.30 ±0.78)	22.79 (22.36 ±0.20)	1.12 (1.12 ±0.01)	72.63 (69.31 ±2.21)	
Air dried	15 mins UVO	Forward	17.73 (17.23 ±0.92)	22.79 (22.40 ±0.17)	1.12 (1.12 ±0.01)	69.25 (68.73 ±3.34)	10
		Reverse	18.62 (17.79 ±0.60)	22.81 (22.36 ±0.18)	1.13 (1.13 ±0.01)	72.17 (70.69 ±1.94)	
Air dried	5 mins O_2 plasma	Forward	16.91 (15.21 ±0.94)	22.17 (22.22 ±0.18)	1.09 (1.02 ±0.04)	70.02 (66.88 ±1.90)	9
		Reverse	18.21 (17.26 ±0.53)	22.20 (22.22 ±0.20)	1.11 (1.07 ±0.03)	73.97 (72.81 ±1.05)	
120 °C 1 min	15 mins UVO	Forward	18.19 (16.86 ±1.29)	22.18 (22.30 ±0.31)	1.14 (1.12 ±0.04)	72.19 (67.70 ±3.93)	8
		Reverse	18.93 (17.98 ±0.86)	22.16 (22.31 ±0.29)	1.14 (1.13 ±0.03)	74.69 (71.50 ±2.28)	
120 °C 1 min	5 mins O_2 plasma	Forward	16.49 (14.47 ±1.72)	21.99 (22.19 ±0.25)	1.05 (1.00 ±0.05)	71.21 (65.01 ±5.38)	9
		Reverse	18.26 (17.15 ±0.82)	21.98 (22.27 ±0.24)	1.09 (1.05 ±0.03)	76.28 (73.21 ±2.34)	

Table S4: Device performances for devices using annealing-free and flash-dried spin-coated np-SnO$_2$ layers. Best cells in both sweep directions are given as well as average and standard deviation.
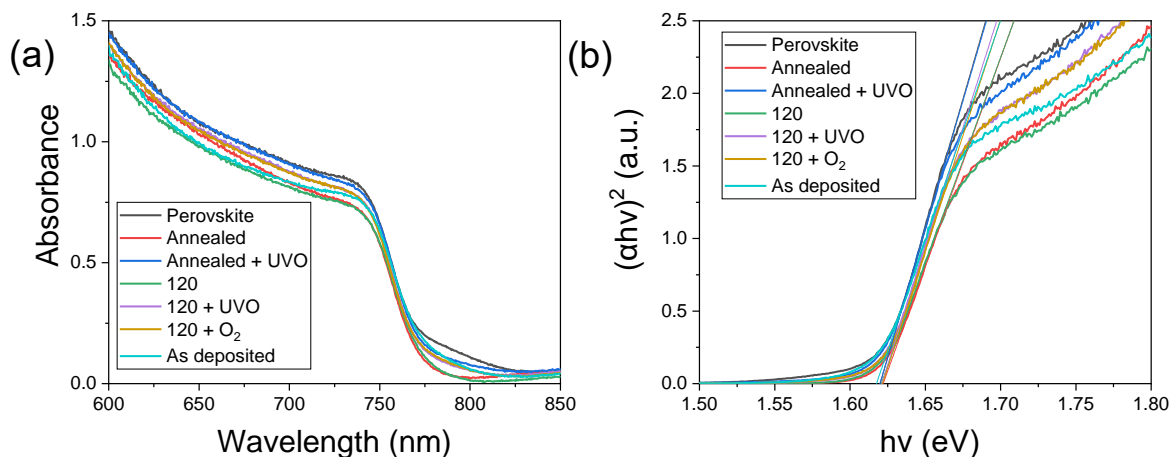
Figure S15: a) Absorbance and b) Tauc plots for np-SnO₂/perovskite interface samples with various np-SnO₂ processing conditions, and comparable optical E_{gap} in all cases (Table S5). A quartz-coated glass/perovskite sample is also shown for reference, with apparent sub-bandgap absorption being a measurement artefact that is likely to lead to a small error in the optical E_{gap} as derived from the Tauc plot.

Figure S16: Normalised PL for np-SnO₂/perovskite interface samples showing no significant changes to the perovskite layer with different interface treatments. Excitation and collection were from the glass side. An extended tail is observed for the quartz-coated glass/perovskite sample, due to improved perovskite film formation on the np-SnO₂ layer.

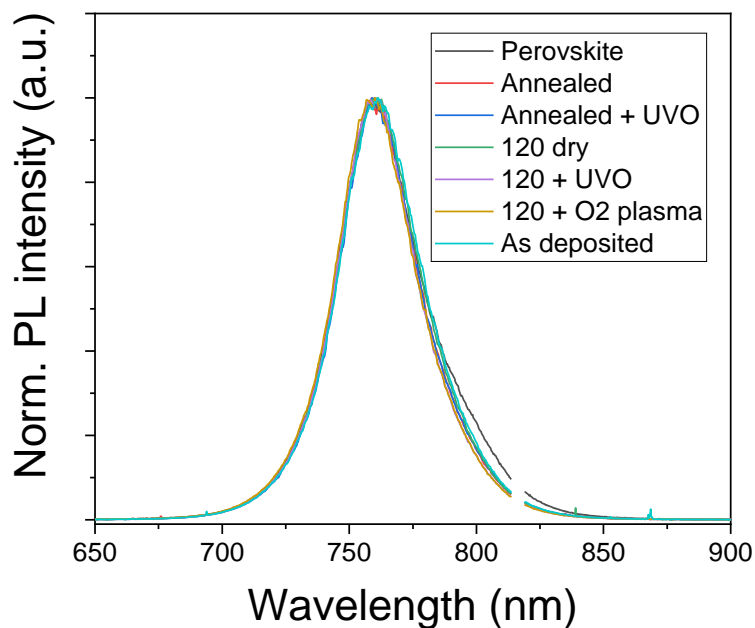| Sample	PL (nm)	PL (eV)	Tauc E_{gap} (nm)	Tauc E_{gap} (eV)
Perovskite	759.9	1.63	765.1	1.62
Annealed	759.9	1.63	764.2	1.62
Annealed + UVO	760.3	1.63	765.3	1.62
As deposited	761.2	1.63	766.3	1.62
As dep + UVO	761.0	1.63	765.2	1.62
As dep + O_2	759.3	1.63	764.4	1.62
120 dry	760.7	1.63	764.9	1.62
120 + UVO	759.6	1.63	764.6	1.62
120 + O_2	759.3	1.63	764.2	1.62

Table S5: Optical E_{gap} determination for perovskite on np-SnO_2 substrates from extrapolation of linear region of Tauc plots (Figure S15) and SSPL measurements (Figure S16) fitted with an exponentially-modified Gaussian.
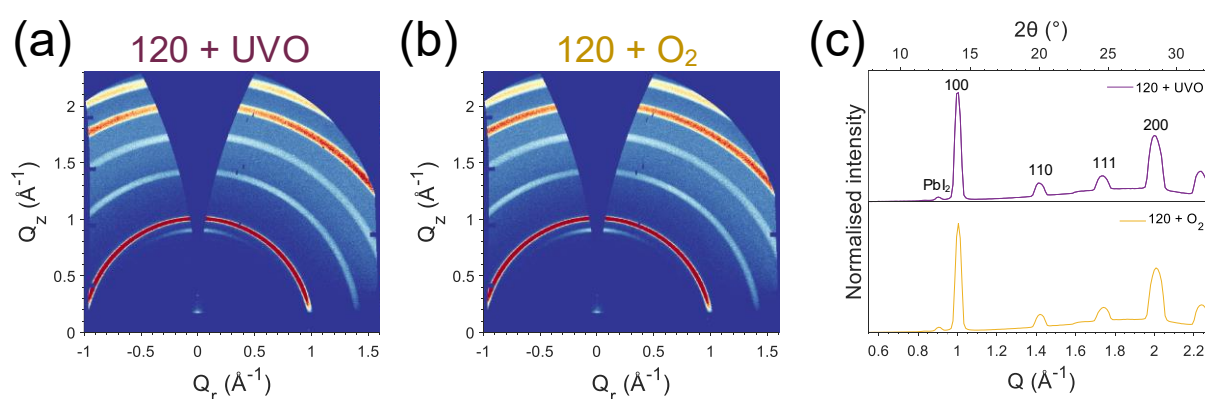
Figure S17: GIWAXS patterns for perovskite layer grown on a) 120 + UVO and b) 120 + O_2 plasma np-SnO_2 layers. c) Azimuthal integrations through the 2D patterns, confirming the presence of some out-of-plane oriented PbI_2 and pseudo-cubic perovskite in both samples, with no observable differences between samples.

Figure S18: pH strip confirming pH of the undiluted np-SnO_2 to be ~11.5, with strong basicity due to KOH stabiliser.
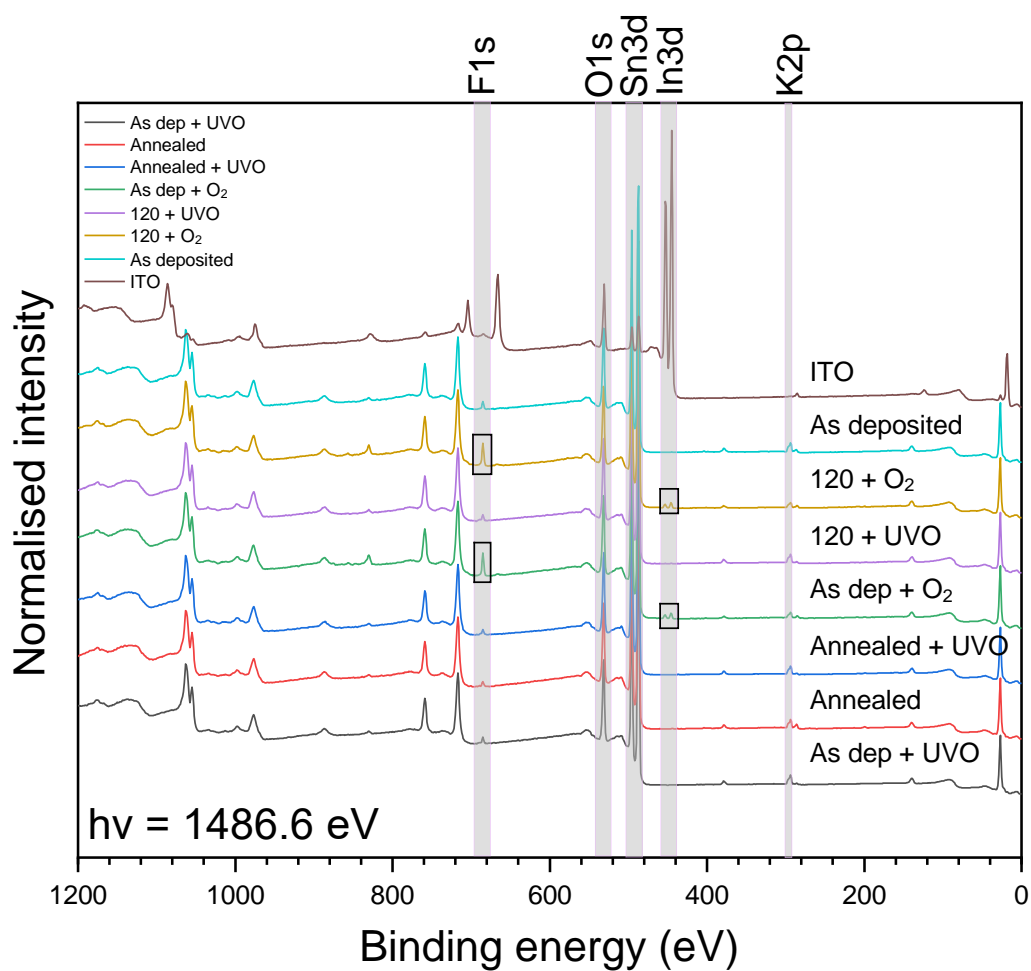
Figure S19: XPS wide scan spectra for all samples. Both 120 + O_2 plasma and 'As deposited + O_2' plasma samples show comparatively increased F 1s and In 3d intensity, with reduced K 2p.
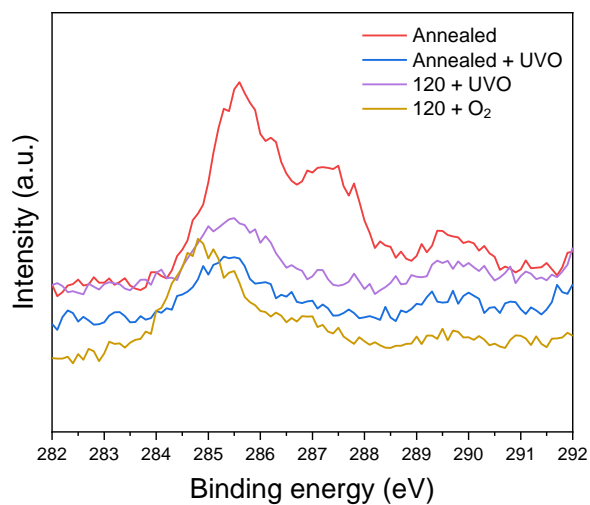
Figure S20: XPS spectra of C 1s core level emission for each process step. We find that UVO and O_2 plasma reduce adventitious carbon at the sample surface.
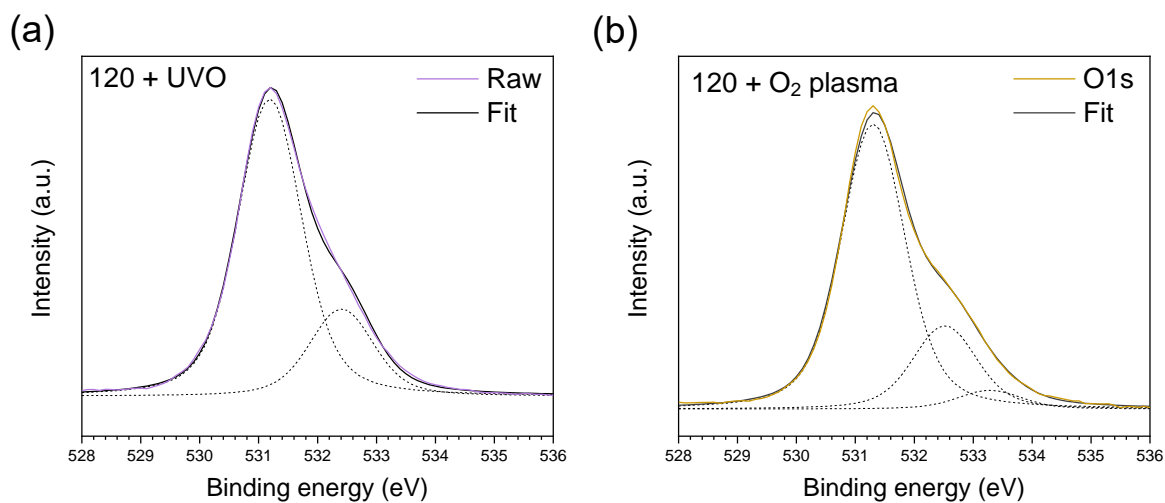
Figure S21: XPS spectra for O 1s core levels for a) 120 + UVO and b) 120 + O_2 plasma samples. Three peaks are required to fit O_2 plasma treated samples, with this third environment ascribed to a contaminant species most likely related to fluorine. The fitting methodology is described in the Experimental Methods section above.

	O 1s peak areas			Area ratios	
Sample	O-Sn	-OH/O$_{ads}$	HES	O-Sn/[Sn 3d]	[O 1s]/[Sn 3d]
Annealed	0.78	0.22		0.45	0.57
Annealed + UVO	0.77	0.23		0.43	0.56
As deposited	0.77	0.23		0.42	0.55
As dep + UVO	0.78	0.22		0.43	0.55
As dep + O$_2$	0.72	0.21	0.07	0.38	0.53
120 + UVO	0.79	0.21		0.44	0.56
120 + O$_2$	0.73	0.22	0.05	0.40	0.54

**Table S6:** Fitted peak areas from XPS O 1s core level spectra for all samples. Two species, ascribed to Sn-O (or lattice oxygen) and -OH/O$_{ads}$ (hydroxides and other adsorbed species) are fitted for all samples. Both O$_2$ plasma treated samples show a third peak (denoted here as high energy shoulder, HES) ascribed to a contaminant species or defect introduced with the fluorine contamination. Both O$_2$ plasma species show a reduction in peak area ratios; O-Sn/[Sn 3d] (comparing Sn 3d area with only the lattice oxygen peak) and [O 1s]/[Sn 3d] (comparing with all O 1s peak areas), which may indicate a more oxygen-deficient surface.
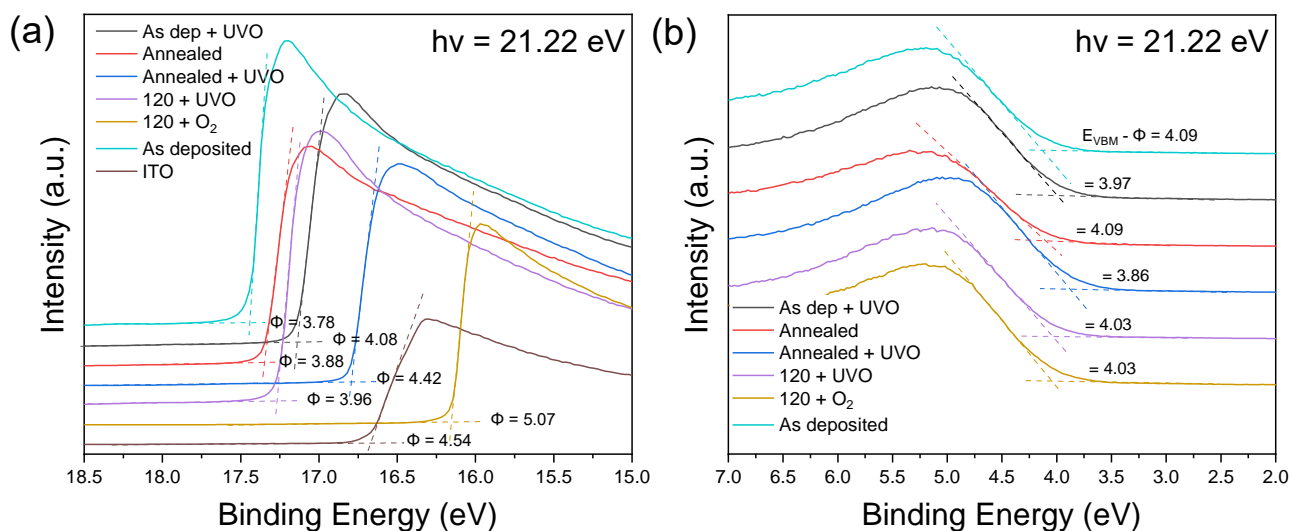

Figure S22: UPS spectra showing a) secondary electron edge with E$_{cutoff}$ measured to determine work function (Φ) and b) E$_{onset}$/E$_B$ to find the valence band maximum.
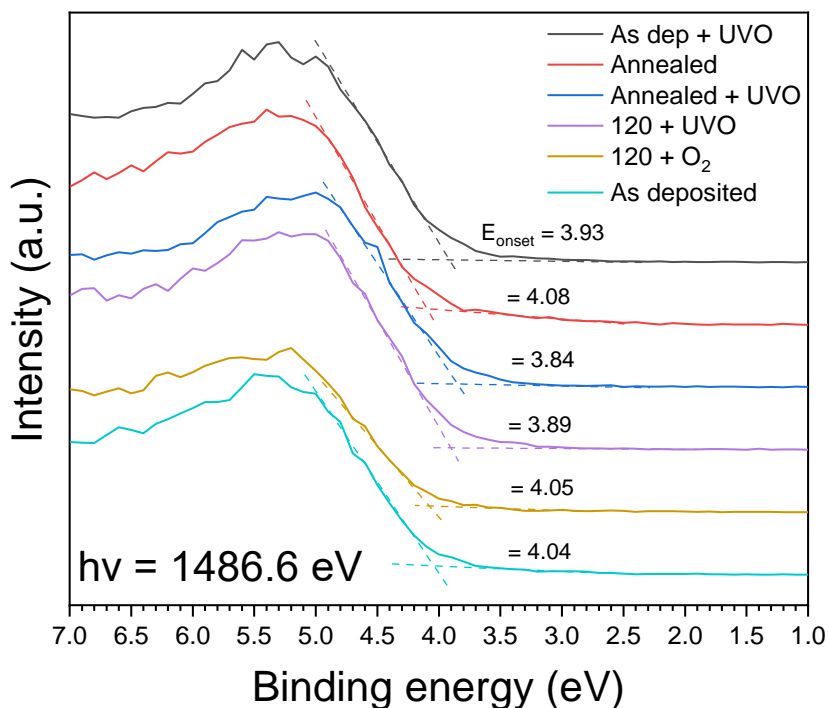
Figure S23: XPS valence spectra used to confirm E_{onset} for IE/valence band determination.

Sample	E_{cutoff} Secondary electron edge	WF Φ	E_{onset} (E_B) UPS	E_{onset} (E_B) XPS	Ionisation energy (IE) UPS	Ionisation energy (IE) XPS	Optical E_{gap}	Estimated electron affinity (EA) UPS	Estimated electron affinity (EA) XPS
SnO$_2$ NPs (literature)[14]		4.36	3.74		8.10		3.79	4.31	
ITO + UVO	16.68	4.54	3.09	3.15	7.64	7.69			
Annealed	17.34	3.88	4.09	4.08	7.96	7.95	4.45	3.51	3.50
Annealed + UVO	16.80	4.42	3.86	3.84	8.29	8.26	4.45	3.84	3.81
As deposited	17.44	3.78	4.09	4.04	7.86	7.82	4.48	3.38	3.34
As dep + UVO	17.14	4.08	3.97	3.93	8.05	8.01	4.48	3.57	3.53
As dep + O$_2$	16.22	5.00	4.04	4.10	9.03	9.10	4.48	4.55	4.62
120 + UVO	17.26	3.96	4.03	3.89	7.99	7.85	4.48	3.51	3.37
120 + O$_2$ plasma	16.15	5.07	4.03	4.05	9.11	9.13	4.48	4.63	4.65

Table S7: Electronic structure of np-SnO$_2$ determined from UPS and XPS measurements, with all energies in eV. EA is estimated using optical E_{gap} (Figure S12). All UPS and XPS values are shown without error due to fitting.

	W.r.t. E_{vac}			W.r.t. E_f		
	VBM (-E_I)	WF (Φ)	CBM (-EA)	VBM	WF	CBM
ITO + UVO		-4.54				
Annealed	-7.96	-3.88	-3.51	-4.08	0	0.37
Annealed + UVO	-8.28	-4.42	-3.83	-3.85	0	0.60
As deposited	-7.84	-3.78	-3.36	-4.06	0	0.42
As dep + UVO	-8.03	-4.08	-3.55	-3.95	0	0.53
As dep + O_2	-9.07	-5.00	-4.59	-4.07	0	0.41
120 + UVO	-7.92	-3.96	-3.44	-3.96	0	0.52
120 + O_2 plasma	-9.12	-5.07	-4.64	-4.04	0	0.44

Table S8: Energy levels used, averaging UPS and XPS, as shown in Figure 6a (with respect to vacuum) and w.r.t. the Fermi level. Values are given without errors related to the fitting.

			Perovskite		spiro-OMeTAD	
Stated composition (reference)	Substrate	Methods	IE (eV)	EA (eV)	IE (eV)	EA (eV)
$Cs_6(MA_{0.17}FA_{0.83})_{94}Pb(I_{0.83}Br_{0.17})_3$ **(15)**	ZnO	UPS/Tauc	6.08	4.46	5.7	2.2
$CsI_{0.05}((FAPbI_3)_{0.87}(MAPbBr_3)_{0.13})_{0.95}$ **(16)**	Unknown	UPS	5.7	est. 4.1	5.4	
$Cs_{0.05}((FAPbI_3)_{0.85}(MAPbBr_3)_{0.15})_{0.95}$ **(17)**	TiO_2	UPS/Tauc	5.4	3.79	5.22	
$Cs_{0.05}FA_{0.79}MA_{0.16}Pb(I_{0.83}Br_{0.17})_3$ **(18)**	PEDOT:PSS	UPS	5.87	4.26		

Table S9: Typical energy level literature values for various triple-cation perovskite compositions and spiro-OMeTAD layers deposited on different transport layers.
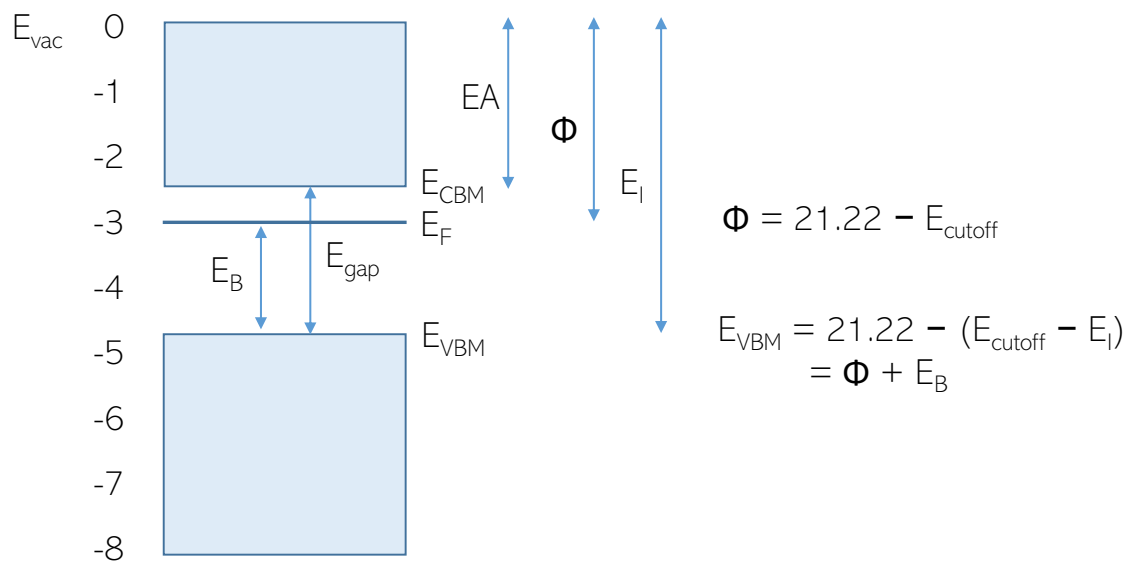
Figure S24: Illustration of energy level determination from UPS measurements.

The energy level diagram shows:

$$\Phi = 21.22 - E_{cutoff}$$

$$E_{VBM} = 21.22 - (E_{cutoff} - E_I)$$
$$= \Phi + E_B$$

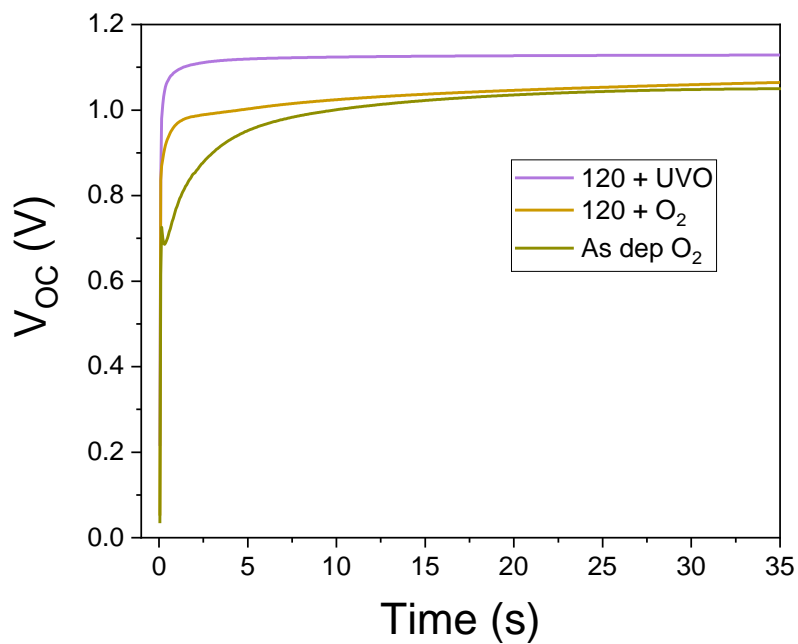Labels: E_{vac}, E_{CBM}, E_F, E_{VBM}, E_B, E_{gap}, EA, Φ, E_I

Figure S25: Transient photovoltage measurements showing the evolution of V_{OC} for completed devices with different np-SnO$_2$ interface treatments, with both O$_2$ plasma treated samples stabilising more gradually.

References

(1)   Ke, W.; Fang, G.; Liu, Q.; Xiong, L.; Qin, P.; Tao, H.; Wang, J.; Lei, H.; Li, B.; Wan, J.; Yang, G.; Yan, Y. Low-Temperature Solution-Processed Tin Oxide as an Alternative Electron Transporting Layer for Efficient Perovskite Solar Cells. *J. Am. Chem. Soc.* **2015**, *137* (21), 6730–6733. https://doi.org/10.1021/jacs.5b01994.

(2)   Anaraki, E. H.; Kermanpur, A.; Steier, L.; Domanski, K.; Matsui, T.; Tress, W.; Saliba, M.; Abate, A.; Grätzel, M.; Hagfeldt, A.; Correa-Baena, J.-P. Highly Efficient and Stable Planar Perovskite Solar Cells by Solution-Processed Tin Oxide. *Energy Environ. Sci.* **2016**, *9* (September), 3128–3134. https://doi.org/10.1039/C6EE02390H.

(3)   Jiang, Z. GIXSGUI: A MATLAB Toolbox for Grazing-Incidence X-Ray Scattering Data Visualization and Reduction, and Indexing of Buried Three-Dimensional Periodic Nanostructured Films. *J. Appl. Crystallogr.* **2015**, *48* (3), 917–926. https://doi.org/10.1107/S1600576715004434.

(4)   SasView software package www.sasview.org.

(5)   Tress, W.; Yavari, M.; Domanski, K.; Yadav, P.; Niesen, B.; Correa Baena, J. P.; Hagfeldt, A.; Graetzel, M. Interpretation and Evolution of Open-Circuit Voltage, Recombination, Ideality Factor and Subgap Defect States during Reversible Light-Soaking and Irreversible Degradation of Perovskite Solar Cells. *Energy Environ. Sci.* **2018**, *11* (1), 151–165. https://doi.org/10.1039/c7ee02415k.

(6)   Guerra, J. A.; Tejada, A.; Korte, L.; Kegelmann, L.; Töfflinger, J. A.; Albrecht, S.; Rech, B.; Weingärtner, R. Determination of the Complex Refractive Index and Optical Bandgap of CH3NH3PbI3 Thin Films. *J. Appl. Phys.* **2017**, *121* (17), 173104. https://doi.org/10.1063/1.4982894.

(7)   Guerra, J. A.; Tejada, A.; Töfflinger, J. A.; Grieseler, R.; Korte, L. Band-Fluctuations Model for the Fundamental Absorption of Crystalline and Amorphous Semiconductors: A Dimensionless Joint Density of States Analysis. *J. Phys. D. Appl. Phys.* **2019**, *52* (10), 105303. https://doi.org/10.1088/1361-6463/aaf963.

(8)   Wojdyr, M. Fityk: A General-Purpose Peak Fitting Program. *J. Appl. Crystallogr.* **2010**, *43* (5 PART 1), 1126–1128. https://doi.org/10.1107/S0021889810030499.

(9)   Bu, T.; Li, J.; Zheng, F.; Chen, W.; Wen, X.; Ku, Z.; Peng, Y.; Zhong, J.; Cheng, Y.-B.; Huang, F. Universal Passivation Strategy to Slot-Die Printed SnO2 for Hysteresis-Free Efficient Flexible

Perovskite Solar Module. *Nat. Commun.* **2018**, *9* (1), 4609. https://doi.org/10.1038/s41467-018-07099-9.

(10)   Wang, Z.; Richter, S. M.; Rozema, M. J.; Schellinger, A.; Smith, K.; Napolitano, J. G. Potential Safety Hazards Associated with Using Acetonitrile and a Strong Aqueous Base. *Org. Process Res. Dev.* **2017**, *21* (10), 1501–1508. https://doi.org/10.1021/acs.oprd.7b00158.

(11)   Bishop, J. E.; Routledge, T. J.; Lidzey, D. G. Advances in Spray-Cast Perovskite Solar Cells. *J. Phys. Chem. Lett.* **2018**, 1977–1984. https://doi.org/10.1021/acs.jpclett.8b00311.

(12)   Henke, B. L.; Gullikson, E. M.; Davis, J. C. X-Ray Interactions: Photoabsorption, Scattering, Transmission, and Reflection at E = 50-30,000 EV, Z = 1-92. *At. Data Nucl. Data Tables* **1993**, *54* (2), 181–342. https://doi.org/10.1006/adnd.1993.1013.

(13)   Hammouda, B. A New Guinier-Porod Model. *J. Appl. Crystallogr.* **2010**, *43* (4), 716–719. https://doi.org/10.1107/S0021889810015773.

(14)   Jiang, Q.; Zhang, L.; Wang, H.; Yang, X.; Meng, J.; Liu, H.; Yin, Z.; Wu, J.; Zhang, X.; You, J. Enhanced Electron Extraction Using SnO2 for High-Efficiency Planar-Structure HC(NH2)2PbI3-Based Perovskite Solar Cells. *Nat. Energy* **2017**, *2* (1), 16177. https://doi.org/10.1038/nenergy.2016.177.

(15)   Song, J.; Liu, L.; Wang, X. F.; Chen, G.; Tian, W.; Miyasaka, T. Highly Efficient and Stable Low-Temperature Processed ZnO Solar Cells with Triple Cation Perovskite Absorber. *J. Mater. Chem. A* **2017**, *5* (26), 13439–13447. https://doi.org/10.1039/c7ta03331a.

(16)   Prochowicz, D.; Tavakoli, M. M.; Kalam, A.; Chavan, R. D.; Trivedi, S.; Kumar, M.; Yadav, P. Influence of A-Site Cations on the Open-Circuit Voltage of Efficient Perovskite Solar Cells: A Case of Rubidium and Guanidinium Additives. *J. Mater. Chem. A* **2019**, *7* (14), 8218–8225. https://doi.org/10.1039/c9ta00272c.

(17)   Deepa, M.; Salado, M.; Calio, L.; Kazim, S.; Shivaprasad, S. M.; Ahmad, S. Cesium Power: Low Cs+levels Impart Stability to Perovskite Solar Cells. *Phys. Chem. Chem. Phys.* **2017**, *19* (5), 4069–4077. https://doi.org/10.1039/c6cp08022g.

(18)   Ji, L.; Zhang, X.; Zhang, T.; Wang, Y.; Wang, F.; Zhong, Z.; Chen, Z. D.; Xiao, Z.; Chen, L.; Li, S. Band Alignment of Pb-Sn Mixed Triple Cation Perovskites for Inverted Solar Cells with Negligible Hysteresis. *J. Mater. Chem. A* **2019**, *7* (15), 9154–9162. https://doi.org/10.1039/c8ta11891d.